The Dimensional Reduction Approach for 2D Non-prismatic Beam Modelling: a Solution Based on Hellinger-Reissner Principle

Ferdinando Auricchio[a], Giuseppe Balduzzi[a,*], Carlo Lovadina[b]

[a] *Dipartimento di Ingengeria Civile e Architettura (DICAr), Università degli Studi di Pavia, via Ferrata 3, 27100 Pavia Italy*
[b] *Dipartimento di Matematica "Felice Casorati", Università degli Studi di Pavia, via Ferrata 1, 27100 Pavia Italy*

Abstract

The present paper considers a non-prismatic beam i.e., a beam with a cross-section varying along the beam axis. In particular, we derive and discuss a model of a 2D linear-elastic non-prismatic beam and the corresponding finite element. To derive the beam model, we use the so-called dimensional reduction approach: from a suitable weak formulation of the 2D linear elastic problem, we introduce a variable cross-section approximation and perform a cross-section integration. The satisfaction of the boundary equilibrium on lateral surfaces is crucial in determining the model accuracy since it leads to consider correct stress-distribution and coupling terms (i.e., equation terms that allow to model the interaction between axial-stretch and bending). Therefore, we assume as a starting point the Hellinger-Reissner functional in a formulation that privileges the satisfaction of equilibrium equations and we use a cross-section approximation that exactly enforces the boundary equilibrium.

The obtained beam-model is governed by linear Ordinary Differential Equations (ODEs) with non-constant coefficients for which an analytical solution cannot be found, in general. As a consequence, starting from the beam model, we develop the corresponding beam finite element approximation. Numerical results show that the proposed beam model and the corresponding finite element are capable to correctly predict displacement and stress distributions in non-trivial cases like tapered and arch-shaped beams.

Keywords: Tapered Beam Modelling, Non-prismatic Beam Modelling, Finite element, Mixed Variational Formulation

*Corresponding author. *Adress*: Dipartimento di Ingengeria Civile e Architettura (DICAr), Università degli Studi di Pavia, via Ferrata 3, 27100 Pavia Italy *Email adress*: `giuseppe.balduzzi@unipv.it` *Phone*: 0039 0382 985 468

Email addresses: `ferdinando.auricchio@unipv.it` (Ferdinando Auricchio), `giuseppe.balduzzi@unipv.it` (Giuseppe Balduzzi), `carlo.lovadina@unipv.it` (Carlo Lovadina)

Nomenclature

E Young's modulus

$H(0), H(\overline{l})$ initial and final cross-sections

$H(x)$ beam cross-section

J_{HR} Hellinger-Reissner (HR) functional

$L^2(\Omega), H(\mathrm{div}, \Omega)$ 2D Sobolev spaces

$L^2(l), H^1(l)$ beam-model Sobolev spaces

$M(x)$ bending moment

$N(x)$ resulting axial stress

O, x, y Cartesian coordinate system

$V(x)$ resulting shear

W, S_0, S_t 2D HR functional spaces

Δ difference of cross-section height

Ω beam body i.e., 2D problem domain

$\delta\boldsymbol{s}, \delta\boldsymbol{\sigma}$ virtual fields

$\frac{\partial}{\partial x}, \frac{\partial}{\partial y}$ $x-$ and $y-$ partial derivatives

γ generic field

γ^{ref} reference solution

$\hat{\boldsymbol{\gamma}}$ axial coefficient functions

$\hat{\boldsymbol{t}}_x, \hat{\boldsymbol{t}}_y$ projection of external load on profile functions

λ wave length

$\nabla \cdot (\cdot)$ divergence operator

ν Poisson's coefficient

$\overline{H}(x)$ cross-section height

$\overline{\boldsymbol{s}}$ boundary displacement function

$\overline{l}$ beam length

$\overline{u}, \overline{v}$ cross-section axial- and transversal- displacement mean-values

$\partial\Omega$ domain boundary

$\partial\Omega_s, \partial\Omega_t$ displacement constrained and externally loaded boundaries

$\boldsymbol{D}$ fourth-order elastic tensor

$\boldsymbol{E}_1, \boldsymbol{E}_2$ engineering notation's Boolean matrices

$\boldsymbol{F}$ beam-model load vector

$\boldsymbol{G}, \boldsymbol{H}$ ODE coefficient matrices

$\boldsymbol{H}_{\sigma s}, \boldsymbol{H}_{\sigma\sigma}, \boldsymbol{G}_{\sigma s}$ beam-model coefficient matrices

$\boldsymbol{K}_{s\sigma}, \boldsymbol{K}_{\sigma\sigma}$ FE stiffness matrices

$\boldsymbol{N}_{\gamma i}$ axis shape functions

$\boldsymbol{P}_s, \boldsymbol{P}_\sigma$ matrices collecting displacement and stress profile functions

$\boldsymbol{R}$ matrix accounting for boundary equilibrium

$\boldsymbol{T}$ beam-model external load vector

$\boldsymbol{\sigma}$ symmetric stress tensor field

$\boldsymbol{f}$ distributed load

$\boldsymbol{n}$ outward unit vector

$\boldsymbol{p}_\gamma$ profile functions

$\boldsymbol{s}$ displacement vector field

$\boldsymbol{t}$ external load distribution

σ_x, σ_y, τ axial, transversal, and shear stresses

$\widetilde{W}, \widetilde{S}$ beam-model variational formulation spaces

$\widetilde{\boldsymbol{T}}$ FE load vector

$\widetilde{\boldsymbol{\gamma}}_i$ numerical coefficients

$e(x)$ eccentricity

e_γ^{rel} relative error

$h_l(x), h_u(x)$ cross section lower- and upper- boundaries

l beam longitudinal axis

m number of profile functions

u, v horizontal and vertical displacements

t number of axis shape functions

1. Introduction

Non-prismatic beams are slender bodies in which the position of the cross-section barycentre, the cross-section shape, and/or the cross-section size vary along the prevalent dimension of the body. Those bodies are widely used in engineering practice since they provide effective solutions for optimisation problems. As an example, arc-shaped beams (in Figure 1(a) the Risorgimento bridge, Verona, Italy) could be optimized in order to carry the loads using the minimum amount of materials. As an other, more sophisticated example, windmill turbine blades (in Figure 1(b) the fiberglass-reinforced epoxy blades of Siemens SWT-2.3-101 wind turbines) are optimized with respect to different conflicting needs like aerodynamic efficiency, noise pollution, forces induced on the tower. The models that describe the behaviour of non-prismatic beams must be as efficient as possible in order to perform an effective design. Unfortunately, non-prismatic beam models rarely satisfy the needs of the practitioners, who must choose between refined but too expensive models –like 3D

(a) Risorgimento bridge, Verona, Italy, designed by eng. Pier Luigi Nervi (1963). The cross-section shape changes in order to maximize the resistance to the bending moment using the minimum amount of material. Image from it.wikipedia.org.

(b) Fiberglass-reinforced epoxy blades of Siemens SWT-2.3-101 wind turbines. Image from it.wikipedia.org.

Figure 1: Examples of structures that could be seen as non-prismatic beams

Finite Element (FE) analysis– and inexpensive but too coarse models –like frame analysis that uses 1D elements with piecewise-constant cross-sections.

Consider first the tapered beams, i.e. a class of non-prismatic beams with the following properties: (i) the beam has a straight axis, (ii) the cross-section dimension varies linearly with respect to the axis coordinate, and (iii) the cross sections have at least two symmetry axes whose intersection coincides with the beam axis. Under these conditions, the positions of either cross-section barycentre (i.e., the point where a resulting axial force can be applied without inducing any bending moment) and shear-centre (i.e., the point where a resulting shear force can be applied without inducing any torsion) do not depend on the beam-axis coordinate. The tapered-beam modelling takes advantage of the tapered-beam geometry since it ensures that axial-, transverse-, and rotation- equilibrium equations are independent. As a consequence of their simplicity, tapered beams are deeply investigated and many modelling approaches have been proposed in the literature, as illustrated in the following. The simplest modelling-approach consists in modifying the coefficients of the Euler-Bernoulli (EB) or Timoshenko beam-model equations in order to take into account the variation of the cross-section area and inertia along the beam axis. Banerjee and Williams (1985, 1986) illustrate significant examples of this modelling approach, used for example in Vinod et al. (2007) as the basis of the FE analysis. Unfortunately, it is well-known that this approach introduces a modelling error proportional to the rate of cross-section size change which is non-negligible also for small rates (see Boley, 1963). Moreover, investigating the effect of the variation of cross-section size, Hodges et al. (2010) show that the model degeneration is a consequence of the violation of the boundary equilibrium on the lateral surface in the beam model formulation.

Extending the discussion to more complex geometries, new difficulties arise. In fact, considering beams without any symmetry with respect to the beam axis, the positions of barycentre and shear centre vary along the beam axis independently of the position of resulting applied loads. In this context, an axial and shear loads respectively produce variable bending- and torque- moments. On the other hand, EB and Timoshenko model axial-, transverse-, and rotation- equilibriums with independent equations, as a consequence they cannot describe such complex effects. To overcome the coupling problems, Li and Li (2002) and Kitipornchai and Trahair (1975) consider the coupling of axial-compression and shear-bending equations, and the coupling of shear-bending and torque equations, respectively, in the case of mono-symmetric cross-sections. Both approaches introduce suitable terms in the model equations. Unfortunately, as highlighted in (Hodges et al., 2010), the evaluation of the coupling term coefficients could be non trivial, in particular for non-trivial cross-section geometries.

In this paper we consider 2D bodies, for which Hodges et al. (2008) develop an effective displacement-based tapered beam model. The authors use the variational-asymptotic method for the model derivation and they consider the slope of the lateral boundary as a model parameter. Starting from this model, Hodges et al. (2010) provide ways to recover stresses and strains, and they have shown the excellent accuracy of the model. More recently, Rajagopal et al. (2012) have used the variational-asymptotic method for the analysis of initially curved isotropic strips, whereas Rajagopal and Hodges (2014) have used the same approach to perform oblique cross-section analysis. In both papers, the proposed approaches lead to accurate and promising results, although the generalization to non-prismatic beams does not seem to be available.

With respect to prismatic 2D beams (i.e., beams with constant cross-section and straight axis), Auricchio et al. (2010) have presented a modelling-approach, based on the dimensional reduction, and a suitable FE approximation of the beam model. The dimensional reduction is a general mathematical procedure, initially proposed by Kantorovich and Krylov (1958), that exploits the domain geometry to reduce the problem dimension (in planar beam modelling from 2D Partial Differential Equations (PDEs) to a system of Ordinary Differential Equations (ODEs)).

This paper generalizes the procedure proposed by Auricchio et al. (2010) to a non-prismatic, homogeneous, linear-elastic planar beam, with the aim to overcome the modelling limitations previously highlighted. In particular, we exploit the capability of the modelling approach described in Auricchio et al. (2010) to accurately capture the cross-section stress distribution.

An brief outline of the paper is as follows.

Section 2 provides a mathematical formulation of the problem under consideration, Section 3 develops the beam model, described by means of an engineering-oriented notation, Section 4 develops the corresponding FE, Section 5 provides some numerical examples, and Section 6 considers the influence of geometry parameters on the beam FE accuracy.

2. 2D-problem variational formulation

We consider a homogeneous, isotropic, and linearly elastic 2D beam Ω with non-constant cross-section. We assume small displacements, small deformations and plane stress state. The beam longitudinal-axis l and the cross-section $H(x)$ are given by

$$l := \left\{ x \in \left[0, \bar{l}\right] \right\}; \quad H(x) := \left\{ y \in \left[h_l(x), h_u(x)\right] \right\} \tag{1}$$

where $\bar{l}$ is the beam length, while $h_l, h_u : l \to \mathbb{R}$ are $C^1(l)$ functions with $h_l(x) < h_u(x)\ \forall x \in l$, which represent the cross section lower and upper boundaries, respectively. Then, we define the problem domain as:

$$\Omega := l \times H(x) \tag{2}$$

As usual in beam modelling, we assume $\bar{l} \gg \overline{H}(x)\ \forall x \in l$, where $\overline{H}(x)$ is the cross section height, defined as $\overline{H}(x) := h_u(x) - h_l(x)$.

Figure 2 represents the domain Ω, the adopted Cartesian coordinate system, the lower and upper boundaries $y = h_l(x)$ and $y = h_u(x)$ respectively, and the initial and final cross sections $H(0)$ and $H\left(\bar{l}\right)$ respectively. We denote the domain boundary as $\partial\Omega := H(0) \cup H\left(\bar{l}\right) \cup h_l(x) \cup h_u(x)$. Moreover, we introduce the partition $\{\partial\Omega_s; \partial\Omega_t\}$, where $\partial\Omega_s$ and $\partial\Omega_t$ are the parts where the displacements $\bar{\boldsymbol{s}} : \partial\Omega_s \to \mathbb{R}^2$ and the tractions $\boldsymbol{t} : \partial\Omega_t \to \mathbb{R}^2$ are imposed, respectively. Finally, we assume that the beam is subjected to a distributed load $\boldsymbol{f} : \Omega \to \mathbb{R}^2$. In what follows, we assume that $\bar{\boldsymbol{s}}$, $\boldsymbol{t}$ and $\boldsymbol{f}$ are sufficiently smooth.

Introducing the displacement vector field $\boldsymbol{s} : \Omega \to \mathbb{R}^2$ and the symmetric stress tensor field $\boldsymbol{\sigma} : \Omega \to \mathbb{R}^{2\times 2}_s$,

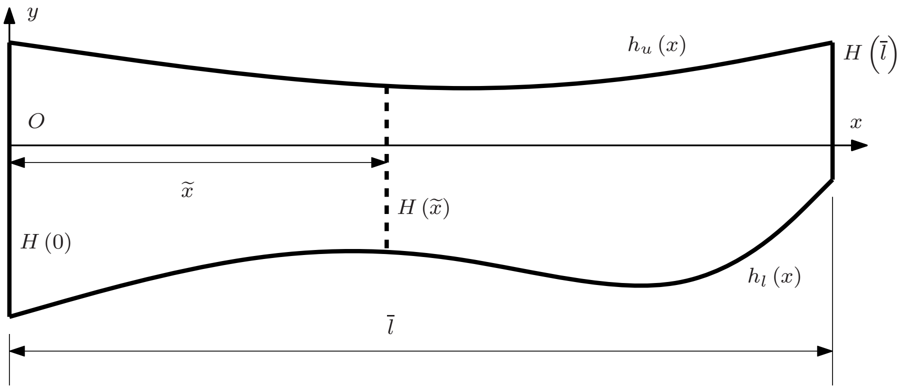

Figure 2: 2D beam geometry, coordinate system, dimensions and adopted notations.

we define the functional spaces W, S_0, and S_t as follows:

$$W := \left\{ \boldsymbol{s} \in L^2(\Omega) \right\} \tag{3}$$

$$S_0 := \left\{ \boldsymbol{\sigma} \in H(\mathrm{div}, \Omega) : \boldsymbol{\sigma} \cdot \boldsymbol{n}|_{\partial\Omega_t} = \boldsymbol{0} \right\} \tag{4}$$

$$S_t := \left\{ \boldsymbol{\sigma} \in H(\mathrm{div}, \Omega) : \boldsymbol{\sigma} \cdot \boldsymbol{n}|_{\partial\Omega_t} = \boldsymbol{t} \right\} \tag{5}$$

where $\boldsymbol{n}$ is the outward unit vector and, being the divergence operator defined as $\nabla \cdot (\,\cdot\,)$, the Sobolev spaces $L^2(\Omega)$ and $H(\mathrm{div}, \Omega)$ are defined as:

$$L^2(\Omega) := \left\{ \boldsymbol{s} : \Omega \to \mathbb{R}^2 \ : \ \int_\Omega \boldsymbol{s} \cdot \boldsymbol{s} \, d\Omega < \infty \right\}$$

$$H(\mathrm{div}, \Omega) := \left\{ \boldsymbol{\sigma} : \Omega \to \mathbb{R}^{2\times 2}_s \ : \ \int_\Omega \boldsymbol{\sigma} : \boldsymbol{\sigma} \, d\Omega < \infty \text{ and } (\nabla \cdot \boldsymbol{\sigma}) \in L^2(\Omega) \right\}$$

Therefore, the 2D problem under investigation can be expressed through the following variational equation.

$$\boxed{\begin{aligned} &\text{Find } \boldsymbol{s} \in W \text{ and } \boldsymbol{\sigma} \in S_t \text{ such that } \forall\, \delta\boldsymbol{s} \in W \text{and } \forall\, \delta\boldsymbol{\sigma} \in S_0 \\ &\delta J_{HR} = -\int_\Omega \delta\boldsymbol{s} \cdot \nabla \cdot \boldsymbol{\sigma} \, d\Omega - \int_\Omega \nabla \cdot \delta\boldsymbol{\sigma} \cdot \boldsymbol{s} \, d\Omega - \int_\Omega \delta\boldsymbol{\sigma} : \boldsymbol{D}^{-1} : \boldsymbol{\sigma} \, d\Omega \\ &\qquad - \int_\Omega \delta\boldsymbol{s} \cdot \boldsymbol{f} \, d\Omega + \int_{\partial\Omega_s} \delta\boldsymbol{\sigma} \cdot \boldsymbol{n} \cdot \overline{\boldsymbol{s}} \, dS = 0 \end{aligned}} \tag{6}$$

where $\boldsymbol{D}$ is the fourth-order, invertible, linear, and elastic tensor, depending on the Young's modulus E and the Poisson's coefficient ν.

We recall that the solution of Equation (6) represents the saddle point of the Hellinger-Reissner (HR) functional J_{HR} (see Auricchio et al., 2010). We highlight also that the displacement constraint $\boldsymbol{s}|_{\partial\Omega_s} = \overline{\boldsymbol{s}}$ is a natural condition i.e., it is weakly imposed through Equation (6), whereas the boundary equilibrium $\boldsymbol{\sigma} \cdot \boldsymbol{n}|_{\partial\Omega_t} = \boldsymbol{t}$ is an essential condition i.e., it is strongly enforced in the trial space S_t (see Equation (5)).

In the following, as usual in beam modelling, we assume that the lower and the upper boundaries are subjected to zero tractions, i.e. $\{h_u(x) \cup h_l(x)\,;\ x \in l\} \subset \partial\Omega_t$ and $\boldsymbol{t}|_{h_l \cup h_u} = \boldsymbol{0}$. Nevertheless, we notice that the latter assumption is could be easily removed without spoiling the model derivation procedure.

The outward normal vectors on the lower and upper boundaries are:

$$
\begin{aligned}
\boldsymbol{n}|_{h_l}(x) &= \frac{1}{\sqrt{1+\left(h_l'(x)\right)^2}} \left\{ \begin{array}{c} h_l'(x) \\ -1 \end{array} \right\} \\
\boldsymbol{n}|_{h_u}(x) &= \frac{1}{\sqrt{1+\left(h_u'(x)\right)^2}} \left\{ \begin{array}{c} -h_u'(x) \\ 1 \end{array} \right\}
\end{aligned}
\tag{7}
$$

where $(\,\cdot\,)'$ means the derivative with respect to x. The boundary equilibrium on lower and upper boundaries (i.e., $(\boldsymbol{\sigma}\cdot\boldsymbol{n})|_{h_l\cup h_u} = \mathbf{0}$) could be expressed as follows:

$$
\left[\begin{array}{cc} \sigma_x & \tau \\ \tau & \sigma_y \end{array} \right] \left\{ \begin{array}{c} n_x \\ n_y \end{array} \right\} = \left\{ \begin{array}{c} 0 \\ 0 \end{array} \right\} \quad \Rightarrow \quad \begin{cases} \sigma_x n_x + \tau n_y = 0 \\ \tau n_x + \sigma_y n_y = 0 \end{cases}
\tag{8}
$$

where we omit to write the restriction operator $(\,\cdot\,)|_{h_l\cup h_u}$ for notation simplicity. Manipulating Equation (8), we express the shear and transversal stresses τ and σ_y as function of the axial stress σ_x. Using definition (7), we obtain the following expressions for the boundary equilibrium:

$$
\tau = -\frac{n_x}{n_y}\sigma_x = h'(x)\,\sigma_x; \qquad \sigma_y = \frac{n_x^2}{n_y^2}\sigma_x = \left(h'(x)\right)^2 \sigma_x
\tag{9}
$$

where $h(x)$ indicates either $h_l(x)$ and $h_u(x)$. Therefore, σ_x could be seen as the independent variable that completely defines the stress state on the upper and the lower boundaries. Moreover, in accordance with (Hodges et al., 2008) and (Hodges et al., 2010), the slopes h_l' and h_u' are sufficient geometric quantities to define the boundary equilibrium.

3. Model derivation

In this section we develop the beam model using the dimensional reduction approach illustrated in Auricchio et al. (2010). However, compared to (Auricchio et al., 2010), the stress cross section approximation is now modified in order to satisfy the boundary equilibrium on the lower and the upper boundaries.

3.1. Profile approximation and notations

Considering a generic field $\gamma : \Omega \to \mathbb{R}^{(\,\cdot\,)}$ involved in the beam models, we introduce its approximation defined as the linear combination of m preassigned linearly independent profile functions $\boldsymbol{p}_\gamma : H(x) \to \mathbb{R}^{(\,\cdot\,)\times m}$, weighted with m undefined axial coefficient functions $\hat{\boldsymbol{\gamma}} : l \to \mathbb{R}^m$. Then, the approximation of a given field $\gamma(x,y)$ is defined as follows:

$$
\gamma(x,y) \approx \boldsymbol{p}_\gamma^T\left(y, h_l(x), h_u(x)\right)\hat{\boldsymbol{\gamma}}(x)
\tag{10}
$$

where $(\,\cdot\,)^T$ is the transpose operator. In what follows, we will usually drop the variables on which the functions depend, for notation simplicity. We remark that, as a consequence of the approximation definition (10), the m components of $\hat{\boldsymbol{\gamma}}$ are the unknowns of the beam model we will develop. In addition, we introduce the following additional hypotheses.

1. The stress profile functions $\boldsymbol{p}_{\sigma_x}$, $\boldsymbol{p}_\tau$, and $\boldsymbol{p}_{\sigma_y}$ are Lagrange polynomials, uniquely defined by the number and the position of suitable interpolating nodes.
2. The lower and upper cross section boundaries $h_l(x)$; $h_u(x)$ are interpolating nodes for the stress profile function.
3. The σ_y and τ profile functions vanish on the lower and upper cross section boundaries i.e., $\forall x \in l \quad \boldsymbol{p}_{\sigma_y}|_{h_l\cup h_u} = \boldsymbol{p}_\tau|_{h_l\cup h_u} = \mathbf{0}$.

Due to definition (10), partial derivatives may be computed as follows:

$$\frac{\partial}{\partial x}\gamma = \frac{\partial}{\partial x}\left(\boldsymbol{p}_\gamma^T\hat{\boldsymbol{\gamma}}\right) = \left(\frac{\partial \boldsymbol{p}_\gamma^T}{\partial h_l}h_l'\hat{\boldsymbol{\gamma}} + \frac{\partial \boldsymbol{p}_\gamma^T}{\partial h_u}h_u'\hat{\boldsymbol{\gamma}}\right) + \boldsymbol{p}_\gamma^T\hat{\boldsymbol{\gamma}}' = \boldsymbol{p}_{\gamma,x}^T\hat{\boldsymbol{\gamma}} + \boldsymbol{p}_\gamma^T\hat{\boldsymbol{\gamma}}'; \qquad \frac{\partial}{\partial y}\gamma = \frac{\partial}{\partial y}\left(\boldsymbol{p}_\gamma^T\hat{\boldsymbol{\gamma}}\right) = \boldsymbol{p}_{\gamma,y}^T\hat{\boldsymbol{\gamma}}$$

where $(\,\cdot\,)'$ indicates x derivative for $\hat{\boldsymbol{\gamma}}$, h_l, and h_l, whereas we use $(\,\cdot\,)_{,x}$ and $(\,\cdot\,)_{,y}$ to denote $x-$ and $y-$ total derivatives for $\boldsymbol{p}_\gamma$, respectively. It is worth noticing that the total derivative with respect to x of $\boldsymbol{p}_\gamma$ vanishes for a prismatic beam. As a consequence, in this case we recover the equations detailed in (Auricchio et al., 2010). Switching to an engineering-oriented notation and considering Equation (10), we set:

$$\boldsymbol{s} = \left\{\begin{array}{c} u\,(x,y) \\ v\,(x,y) \end{array}\right\} \approx \left[\begin{array}{cc} \boldsymbol{p}_u^T & \boldsymbol{0} \\ \boldsymbol{0} & \boldsymbol{p}_v^T \end{array}\right]\left\{\begin{array}{c} \hat{\boldsymbol{u}} \\ \hat{\boldsymbol{v}} \end{array}\right\} = \boldsymbol{P}_s\hat{\boldsymbol{s}} \tag{11}$$

$$\boldsymbol{\sigma} = \left\{\begin{array}{c} \sigma_x(x,y) \\ \sigma_y(x,y) \\ \tau(x,y) \end{array}\right\} \approx \left[\begin{array}{ccc} \boldsymbol{p}_{\sigma_x}^T & \boldsymbol{0} & \boldsymbol{0} \\ \boldsymbol{p}_{\sigma_x}^T\boldsymbol{R}^2 & \boldsymbol{p}_{\sigma_y}^T & \boldsymbol{0} \\ \boldsymbol{p}_{\sigma_x}^T\boldsymbol{R} & \boldsymbol{0} & \boldsymbol{p}_\tau^T \end{array}\right]\left\{\begin{array}{c} \hat{\boldsymbol{\sigma}}_x \\ \hat{\boldsymbol{\sigma}}_y \\ \hat{\boldsymbol{\tau}} \end{array}\right\} = \boldsymbol{P}_\sigma\hat{\boldsymbol{\sigma}} \tag{12}$$

where $\boldsymbol{R}$ is a diagonal matrix whose entries are defined as follows:

$$R_{ii} := \begin{cases} 0 & \text{if} \quad p_{\sigma_x i}|_{h_l} = p_{\sigma_x i}|_{h_u} = 0 \\ h_l' & \text{if} \quad p_{\sigma_x i}|_{h_l} \neq 0 \\ h_u' & \text{if} \quad p_{\sigma_x i}|_{h_u} \neq 0 \end{cases} \tag{13}$$

We highlight that the boundary equilibrium (9) is exactly enforced on the lower and the upper boundaries. Virtual fields are analogously defined as:

$$\delta\boldsymbol{s} = \boldsymbol{P}_s\delta\hat{\boldsymbol{s}}; \quad \delta\boldsymbol{\sigma} = \boldsymbol{P}_\sigma\delta\hat{\boldsymbol{\sigma}}$$

In accordance with the engineering notation just introduced, Table 1 defines the divergence operator and the outward unit vector scalar product. We highlight that products between partial derivatives and Boolean matrices $\boldsymbol{E}_i$, $i = 1, 2$ must be intended as scalar-matrix products, whereas differential operators are applied to the stress approximations $\boldsymbol{P}_\sigma\hat{\boldsymbol{\sigma}}$.

Tensorial notation	Engineering notation
$\nabla\cdot\boldsymbol{\sigma}$	$\left(\frac{\partial}{\partial x}\boldsymbol{E}_1 + \frac{\partial}{\partial y}\boldsymbol{E}_2\right)\boldsymbol{P}_\sigma\hat{\boldsymbol{\sigma}}$
$\boldsymbol{\sigma}\cdot\boldsymbol{n}$	$\left(n_x\boldsymbol{E}_1 + n_y\boldsymbol{E}_2\right)\boldsymbol{P}_\sigma\hat{\boldsymbol{\sigma}}$

Table 1: Tensor and engineering equivalent notations.

The matrices $\boldsymbol{E}_1$ and $\boldsymbol{E}_2$ are defined as follows:

$$\boldsymbol{E}_1 := \left[\begin{array}{ccc} 1 & 0 & 0 \\ 0 & 0 & 1 \end{array}\right]; \qquad \boldsymbol{E}_2 := \left[\begin{array}{ccc} 0 & 0 & 1 \\ 0 & 1 & 0 \end{array}\right]$$

Finally, the fourth order elastic tensor $\boldsymbol{D}^{-1}$ can be expressed as the square matrix:

$$\boldsymbol{D}^{-1} := \frac{1}{E}\left[\begin{array}{ccc} 1 & -\nu & 0 \\ -\nu & 1 & 0 \\ 0 & 0 & 2\,(1+\nu) \end{array}\right]$$

3.2. Dimension reduction

In the following, we assume that $\partial\Omega_s = H(0)$ and $\overline{\boldsymbol{s}} = \boldsymbol{0}$. As a consequence, $\partial\Omega_t = H(\overline{l}) \cup h_l(x) \cup h_u(x)$. In Section 2, we assumed $\boldsymbol{t}|_{h_l \cup h_u} = \boldsymbol{0}$. Here, we suppose also that $\boldsymbol{t}|_{H_l}$ can be exactly represented using the profiles chosen for $\boldsymbol{\sigma}\cdot\boldsymbol{n}$ in order to exactly satisfy the boundary condition. Recalling Definition (12), and noting that $\boldsymbol{n}|_{H_l} = (1,0)^T$, the exact representation of $\boldsymbol{t}|_{H_l}$ implies that there exist suitable vectors $\hat{\boldsymbol{t}}_x$ and $\hat{\boldsymbol{t}}_y$ such that:

$$\boldsymbol{t} = \left\{ \begin{array}{c} \boldsymbol{P}_{\sigma_x}^T \hat{\boldsymbol{t}}_x \\ \boldsymbol{P}_{\tau}^T \hat{\boldsymbol{t}}_y \end{array} \right\} \tag{14}$$

Therefore, the boundary condition $\boldsymbol{\sigma}\cdot\boldsymbol{n}|_{H_l} = \boldsymbol{t}$ may be written as:

$$\left\{ \begin{array}{c} \hat{\boldsymbol{\sigma}}_x(\overline{l}) \\ \hat{\boldsymbol{\tau}}(\overline{l}) \end{array} \right\} = \left\{ \begin{array}{c} \hat{\boldsymbol{t}}_x \\ \hat{\boldsymbol{t}}_y \end{array} \right\} \tag{15}$$

Substituting Equations (11) and (12) in Equation (6) and assuming $\overline{\boldsymbol{s}} = \boldsymbol{0}$, the variational Equation (6) becomes:

$$\begin{aligned} \delta J_{HR} = &- \int_\Omega \delta\hat{\boldsymbol{s}}^T \boldsymbol{P}_s^T \left[\left(\frac{\partial}{\partial x}\boldsymbol{E}_1 + \frac{\partial}{\partial y}\boldsymbol{E}_2 \right) (\boldsymbol{P}_\sigma \hat{\boldsymbol{\sigma}}) \right] d\Omega \\ &- \int_\Omega \left[\left(\frac{\partial}{\partial x}\boldsymbol{E}_1 + \frac{\partial}{\partial y}\boldsymbol{E}_2 \right) (\boldsymbol{P}_\sigma \delta\hat{\boldsymbol{\sigma}}) \right]^T \boldsymbol{P}_s \hat{\boldsymbol{s}}\, d\Omega \\ &- \int_\Omega \delta\hat{\boldsymbol{\sigma}}^T \boldsymbol{P}_\sigma^T \boldsymbol{D}^{-1} \boldsymbol{P}_\sigma \hat{\boldsymbol{\sigma}}\, d\Omega - \int_\Omega \delta\hat{\boldsymbol{s}}^T \boldsymbol{P}_s^T \boldsymbol{f}\, d\Omega = 0 \end{aligned} \tag{16}$$

which can be written as:

$$\begin{aligned} \delta J_{HR} = &- \int_\Omega \left(\delta\hat{\boldsymbol{s}}^T \left(\boldsymbol{P}_s^T \boldsymbol{E}_1 \boldsymbol{P}_\sigma\right) \hat{\boldsymbol{\sigma}}' + \delta\hat{\boldsymbol{s}}^T \left(\boldsymbol{P}_s^T \boldsymbol{E}_1 \boldsymbol{P}_{\sigma,x}\right) \hat{\boldsymbol{\sigma}} + \delta\hat{\boldsymbol{s}}^T \left(\boldsymbol{P}_s^T \boldsymbol{E}_2 \boldsymbol{P}_{\sigma,y}\right) \hat{\boldsymbol{\sigma}} \right) d\Omega \\ &- \int_\Omega \left(\delta\hat{\boldsymbol{\sigma}}'^T \left(\boldsymbol{P}_\sigma^T \boldsymbol{E}_1^T \boldsymbol{P}_s\right) \hat{\boldsymbol{s}} + \delta\hat{\boldsymbol{\sigma}}^T \left(\boldsymbol{P}_{\sigma,x}^T \boldsymbol{E}_1^T \boldsymbol{P}_s\right) \hat{\boldsymbol{s}} + \delta\hat{\boldsymbol{\sigma}}^T \left(\boldsymbol{P}_{\sigma,y}^T \boldsymbol{E}_2^T \boldsymbol{P}_s\right) \hat{\boldsymbol{s}} \right) d\Omega \\ &- \int_\Omega \delta\hat{\boldsymbol{\sigma}}^T \left(\boldsymbol{P}_\sigma^T \boldsymbol{D}^{-1} \boldsymbol{P}_\sigma\right) \hat{\boldsymbol{\sigma}}\, d\Omega - \int_\Omega \delta\hat{\boldsymbol{s}}^T \left(\boldsymbol{P}_s^T \boldsymbol{f}\right) d\Omega = 0 \end{aligned} \tag{17}$$

Recalling that only the profile functions depend on y, using Fubini-Tonelli Theorem and integrating over $H(x)$, Equation (17) becomes:

$$\begin{aligned} \delta J_{HR} = \int_l \Big(&- \delta\hat{\boldsymbol{s}}^T \boldsymbol{G}_{s\sigma} \hat{\boldsymbol{\sigma}}' - \delta\hat{\boldsymbol{s}}^T \boldsymbol{H}_{s\sigma} \hat{\boldsymbol{\sigma}} - \delta\hat{\boldsymbol{\sigma}}'^T \boldsymbol{G}_{\sigma s} \hat{\boldsymbol{s}} - \delta\hat{\boldsymbol{\sigma}}^T \boldsymbol{H}_{\sigma s} \hat{\boldsymbol{s}} \\ &- \delta\hat{\boldsymbol{\sigma}}^T \boldsymbol{H}_{\sigma\sigma} \hat{\boldsymbol{\sigma}} - \delta\hat{\boldsymbol{s}}^T \boldsymbol{F} \Big) dx = 0 \end{aligned} \tag{18}$$

where

$$\begin{aligned} &\boldsymbol{H}_{\sigma s} = \boldsymbol{H}_{s\sigma}^T := \int_{H(x)} \left(\boldsymbol{P}_{\sigma,x}^T \boldsymbol{E}_1^T \boldsymbol{P}_s + \boldsymbol{P}_{\sigma,y}^T \boldsymbol{E}_2^T \boldsymbol{P}_s \right) dy; \qquad \boldsymbol{F} := \int_{H(x)} \boldsymbol{P}_s^T \boldsymbol{f} dy; \\ &\boldsymbol{H}_{\sigma\sigma} := \int_{H(x)} \boldsymbol{P}_\sigma^T \boldsymbol{D}^{-1} \boldsymbol{P}_\sigma dy; \qquad \boldsymbol{G}_{\sigma s} = \boldsymbol{G}_{s\sigma}^T := \int_{H(x)} \boldsymbol{P}_\sigma^T \boldsymbol{E}_1^T \boldsymbol{P}_s dy \end{aligned} \tag{19}$$

Equation (18) represents the weak formulation of the 1D beam model. We highlight that the matrices $\boldsymbol{G}_{\sigma s}$, $\boldsymbol{H}_{\sigma s}$, and $\boldsymbol{H}_{\sigma\sigma}$ implicitly depend on x due to the definitions of the profile function and integral domain.

To obtain the boundary value problem of the beam model, we integrate by parts the third term of Equation (18):

$$- \int_l \delta\hat{\boldsymbol{\sigma}}'^T \boldsymbol{G}_{\sigma s} \hat{\boldsymbol{s}} dx = - \delta\hat{\boldsymbol{\sigma}}^T \boldsymbol{G}_{\sigma s} \hat{\boldsymbol{s}} \Big|_{x=0}^{x=\overline{l}} + \int_l \delta\hat{\boldsymbol{\sigma}}^T \boldsymbol{G}'_{\sigma s} \hat{\boldsymbol{s}} dx + \int_l \delta\hat{\boldsymbol{\sigma}}^T \boldsymbol{G}_{\sigma s} \hat{\boldsymbol{s}}' dx \tag{20}$$

Substituting Equation (20) in Equation (18), recalling that $\delta\hat{\boldsymbol{\sigma}} = \mathbf{0}$ on $\partial\Omega_t$ (see Definition (4)), and collecting the axial coefficient functions in a vector, we obtain:

$$\int_l \{\delta\hat{\boldsymbol{s}};\delta\hat{\boldsymbol{\sigma}}\}^T \left(\boldsymbol{G}\left\{\begin{array}{c}\hat{\boldsymbol{s}}'\\ \hat{\boldsymbol{\sigma}}'\end{array}\right\}+\boldsymbol{H}\left\{\begin{array}{c}\hat{\boldsymbol{s}}\\ \hat{\boldsymbol{\sigma}}\end{array}\right\}-\left\{\begin{array}{c}\boldsymbol{F}\\ \mathbf{0}\end{array}\right\}\right)dx+\delta\hat{\boldsymbol{\sigma}}^T\boldsymbol{G}_{\sigma s}\hat{\boldsymbol{s}}\Big|_{H(0)}=0 \tag{21}$$

where

$$\boldsymbol{G} := \left[\begin{array}{cc}\mathbf{0} & -\boldsymbol{G}_{s\sigma}\\ +\boldsymbol{G}_{\sigma s} & \mathbf{0}\end{array}\right]; \qquad \boldsymbol{H} := \left[\begin{array}{cc}\mathbf{0} & -\boldsymbol{H}_{s\sigma}\\ \boldsymbol{G}'_{\sigma s}-\boldsymbol{H}_{\sigma s} & -\boldsymbol{H}_{\sigma\sigma}\end{array}\right]$$

Since Equation (21) must be satisfied by every variations, we finally obtain the following ODEs, equipped with both natural and essential boundary-conditions:

$$\begin{cases}\boldsymbol{G}\left\{\begin{array}{c}\hat{\boldsymbol{s}}'\\ \hat{\boldsymbol{\sigma}}'\end{array}\right\}+\boldsymbol{H}\left\{\begin{array}{c}\hat{\boldsymbol{s}}\\ \hat{\boldsymbol{\sigma}}\end{array}\right\}=\left\{\begin{array}{c}\boldsymbol{F}\\ \mathbf{0}\end{array}\right\} & \text{in } \; l\\ \boldsymbol{G}_{\sigma s}\hat{\boldsymbol{s}}=\mathbf{0} & \text{at } \; x=0\\ \hat{\boldsymbol{\sigma}}_x=\hat{\boldsymbol{t}}_x & \text{at } \; x=\bar{l}\\ \hat{\boldsymbol{\tau}}=\hat{\boldsymbol{t}}_y & \text{at } \; x=\bar{l}\end{cases} \tag{22}$$

It is worth noting that $\boldsymbol{G}_{s\sigma}$ and $\boldsymbol{H}_{s\sigma}$ concern with the beam equilibrium, $\boldsymbol{G}_{\sigma s}$, $\boldsymbol{G}'_{\sigma s}$, and $\boldsymbol{H}_{\sigma s}$ concern with the beam compatibility, and $\boldsymbol{H}_{\sigma\sigma}$ concerns with the beam constitutive laws.

To complete the beam model definition, we choose the profiles $\boldsymbol{p}_\gamma$ as polynomial functions with respect to y of degree at most $\deg(\boldsymbol{p}_\gamma)$, according to Table (2). The same polynomial degrees was adopted in (Auricchio et al., 2010) to model prismatic beams.

	$\boldsymbol{p}_u$	$\boldsymbol{p}_v$	$\boldsymbol{p}_{\sigma_x}$	$\boldsymbol{p}_{\sigma_y}$	$\boldsymbol{p}_\tau$
$\deg(\boldsymbol{p}_\gamma)$	1	2	1	3	2

Table 2: Highest polynomial degree with respect to y of the profile functions used in beam modelling.

It is now possible to compute the matrices $\boldsymbol{G}$ and $\boldsymbol{H}$ for a general non-prismatic beam, for instance with the aid of a symbolic calculus software like MAPLE. We notice that $\text{rank}(\boldsymbol{G}) = 6$, whereas the model uses 10 independent unknowns. As a consequence, we infer that the beam model (22) is a differential-algebraic boundary value problem. Thus, 6 unknowns are determined as a solution of a differential problem, while the remaining 4 are algebraically determined by the former ones. Since $\boldsymbol{G}$ and $\boldsymbol{H}$ are matrices of non-constant coefficients, it is not possible to analytically find the homogeneous solution of the differential equation for a general non-prismatic beam.

Moreover, looking at the definition of the matrix $\boldsymbol{H}_{\sigma s}$ given in Equation (18), we observe that the former term of the integral ($\boldsymbol{P}^T_{\sigma,x}\boldsymbol{E}_1\boldsymbol{P}_s$) vanishes for a prismatic beam, whereas the latter ($\boldsymbol{P}^T_{\sigma,y}\boldsymbol{E}_2\boldsymbol{P}_s$) never vanishes. As a consequence, we conclude that the non-prismatic beam model increases the fill-in of the matrices, i.e., introduces new terms which take into account the axial-bending coupling.

3.3. Coefficient matrices for a symmetric tapered beam

In this section we present a simple beam-model example that highlights the features of the proposed approaches. In particular, we provide the analytical expression of the coefficient matrices $\boldsymbol{G}_{s\sigma}$, $\boldsymbol{H}_{s\sigma}$, and $\boldsymbol{H}_{\sigma\sigma}$ for the symmetric tapered beam depicted in Figure 3. According with the notation of Figure 3, the cross-section lower and upper boundaries and their derivatives are defined by:

$$h_l(x) = -h_u(x) = -\frac{\overline{H}(0)}{2}+\frac{\overline{H}(0)-\overline{H}(\bar{l})}{2\bar{l}}x, \quad h'_l(x) = -h'_u(x) = h' = \frac{\overline{H}(0)-\overline{H}(\bar{l})}{2\bar{l}} \tag{23}$$

We use the following displacement profile functions:

$$\boldsymbol{p}_u = \left\{1; \quad y-\frac{h_l(x)+h_u(x)}{2}\right\}^T; \quad \boldsymbol{p}_v = \left\{1; \quad y-\frac{h_l(x)+h_u(x)}{2}; \quad y^2\right\}^T \tag{24}$$

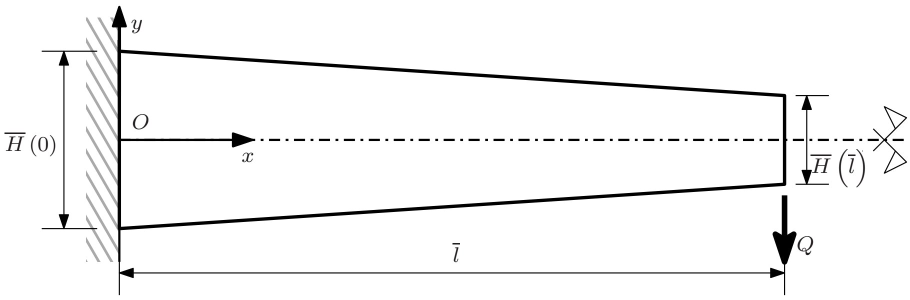

Figure 3: Symmetric tapered beam: $\overline{l} = 10\text{mm}$, $\overline{H}(0) = 1\text{mm}$, $\overline{H}\left(\overline{l}\right) = 0.5\text{mm}$, $Q = 1\text{N}$, $E = 10^5\text{MPa}$, and $\nu = 0.25$.

Therefore, the displacement axial coefficients have specific physical interpretations, as listed in the following.

- $\hat{u}_1$ is the axial displacement mean-value.
- $\hat{u}_2$ is the cross section rotation.
- $\hat{v}_1$ is transversal displacement mean-value.
- $\hat{v}_2$ is a displacement of the cross section, associated to the change of cross-section height.
- $\hat{v}_3$ is a displacement of the cross section, associated to a non uniform deformation.

Moreover, we use the following stress profile functions:

$$\begin{aligned}
\boldsymbol{p}_{\sigma_x} &= \left\{ \frac{h_u(x) - y}{\overline{H}(x)}; \quad \frac{y - h_l(x)}{\overline{H}(x)} \right\}^T; \quad \boldsymbol{p}_\tau = \{4\, p_{\sigma_x 1}\, p_{\sigma_x 2}\} \\
\boldsymbol{p}_{\sigma_y} &= \frac{3\overline{H}(x)^3}{32} \left\{ \begin{array}{c} (y - h_l(x))(h_u(x) - y)\left(y - \left(h_l(x) + \frac{1}{4}\overline{H}(x)\right)\right) \\ (y - h_l(x))(y - h_u(x))\left(y - \left(h_l(x) + \frac{3}{4}\overline{H}(x)\right)\right) \end{array} \right\}
\end{aligned} \tag{25}$$

Therefore, the stress axial coefficients have the physical meanings listed in the following.

- $\hat{\sigma}_{x1}$ is the value of the axial stress at the bottom of the cross section.
- $\hat{\sigma}_{x2}$ is the value of the axial stress at the top of the cross section.
- $\hat{\tau}_1$ is a quadratic bubble function that vanishes on lower and upper cross section boundaries.
- $\hat{\sigma}_{y1}$ and $\hat{\sigma}_{y2}$ are two cubic bubble functions that vanish on lower and upper cross section boundaries.

Inserting all these assumptions in Definitions (19), we obtain the following analytical expressions for the coefficient matrices:

$$
\boldsymbol{G}_{s\sigma} = \overline{H}(x) \begin{bmatrix} 1 & 1 & 0 & 0 & 0 \\ -\frac{1}{3}\overline{H}(x) & \frac{1}{3}\overline{H}(x) & 0 & 0 & 0 \\ h' & -h' & 0 & 0 & \frac{4}{3} \\ -\frac{1}{3}h'\overline{H}(x) & -\frac{1}{3}h'\overline{H}(x) & 0 & 0 & 0 \\ \frac{1}{3}h'\overline{H}^2(x) & -\frac{1}{3}h'\overline{H}^2(x) & 0 & 0 & -\frac{4}{15}\overline{H}^2(x) \end{bmatrix}
$$

$$
\boldsymbol{H}_{s\sigma} = \begin{bmatrix} -h' & -h' & 0 & 0 & 0 \\ -\frac{1}{3}h'\overline{H}(x) & \frac{1}{3}h'\overline{H}(x) & 0 & 0 & -\frac{4}{3}\overline{H}(x) \\ -(h')^2 & (h')^2 & 0 & 0 & -\frac{4}{3}h' \\ -\frac{1}{3}(h')^2\overline{H}(x) & -\frac{1}{3}(h')^2\overline{H}(x) & -\frac{8}{9}\overline{H}(x) & -\frac{8}{9}\overline{H}(x) & 0 \\ -\frac{1}{3}(h')^2\overline{H}^2(x) & \frac{1}{3}(h')^2\overline{H}^2(x) & -\frac{32}{45}\overline{H}^2(x) & \frac{32}{45}\overline{H}^2(x) & -\frac{4}{5}h'\overline{H}^2(x) \end{bmatrix} \tag{26}
$$

$$
\boldsymbol{H}_{\sigma\sigma} = \frac{\overline{H}(x)}{3E} \begin{bmatrix} 2\left((h')^2+1\right)^2 & \left((h')^2-1\right)^2 - 4\nu(h')^2 & \frac{4}{5}\left((h')^2-\nu\right) & \frac{28}{15}\left((h')^2-\nu\right) & 4h'(1+\nu) \\ \left((h')^2-1\right)^2 - 4\nu(h')^2 & 2\left((h')^2+1\right)^2 & \frac{28}{5}\left((h')^2-\nu\right) & \frac{4}{5}\left((h')^2-\nu\right) & -4h'(1+\nu) \\ \frac{4}{5}\left((h')^2-\nu\right) & \frac{28}{15}\left((h')^2-\nu\right) & \frac{704}{315} & \frac{64}{105} & 0 \\ \frac{28}{15}\left((h')^2-\nu\right) & \frac{4}{5}\left((h')^2-\nu\right) & \frac{64}{105} & \frac{704}{315} & 0 \\ 4h'(1+\nu) & -4h'(1+\nu) & 0 & 0 & \frac{32}{5}(1+\nu) \end{bmatrix}
$$

It is worth noting that:

1. For a prismatic beam the lower and upper boundary slopes h' vanish and the cross section height $\overline{H}(x)$ becomes a constant parameter, recovering the single-layer beam model presented in (Auricchio et al., 2010, Section 5.2).
2. Looking at the $\boldsymbol{G}_{s\sigma}$ pattern, the third and the fourth columns have zero entries. As a consequence, derivatives of $\hat{\sigma}_{y1}$ and $\hat{\sigma}_{y2}$ never appear in beam model ODEs; furthermore, the eighth and the ninth equations do not use axial coefficient function derivatives, resulting in algebraic equations. These observations confirm that Equation (22) is a differential-algebraic boundary value problem.
3. Looking at the $\boldsymbol{H}_{\sigma\sigma}$ pattern, the last column and row have non-vanishing entries. As a consequence, we can conclude that, in non-prismatic beam model, the constitutive law introduces coupling between axial deformations and shear stress. These relations represent further equation couplings for which, to the best of the authors' knowledge, no reference in literature exists.

4. FE derivation

We now derive a FEM approximation of our beam model. We first introduce a suitable weak form, as described below.

We integrate by parts with respect to x both the third and the first terms of Equation (18), see Equations (20) and (27).

$$
-\int_l \delta\hat{\boldsymbol{s}}^T \boldsymbol{G}_{s\sigma}\hat{\boldsymbol{\sigma}}' dx = -\delta\hat{\boldsymbol{s}}^T \boldsymbol{G}_{s\sigma}\hat{\boldsymbol{\sigma}}\Big|_{x=0}^{x=\bar{l}} + \int_l \delta\hat{\boldsymbol{s}}^T \boldsymbol{G}'_{s\sigma}\hat{\boldsymbol{\sigma}} dx + \int_l \delta\hat{\boldsymbol{s}}'^T \boldsymbol{G}_{s\sigma}\hat{\boldsymbol{\sigma}} dx \tag{27}
$$

Substituting Equations (20) and (27) into Equation (18), we obtain the variational formulation:

$$\boxed{\begin{aligned}&\text{Find } \hat{\boldsymbol{s}} \in \widetilde{W} \text{ and } \hat{\boldsymbol{\sigma}} \in \widetilde{S} \text{ such that } \forall\, \delta\hat{\boldsymbol{s}} \in \widetilde{W} \text{ and } \forall\, \delta\hat{\boldsymbol{\sigma}} \in \widetilde{S}\\ &\delta J_{HR} = \int_l \Big(\delta\hat{\boldsymbol{s}}'^T \boldsymbol{G}_{s\sigma}\hat{\boldsymbol{\sigma}} + \delta\hat{\boldsymbol{s}}^T \boldsymbol{G}'_{s\sigma}\hat{\boldsymbol{\sigma}} - \delta\hat{\boldsymbol{s}}^T \boldsymbol{H}_{s\sigma}\hat{\boldsymbol{\sigma}} + \delta\hat{\boldsymbol{\sigma}}^T \boldsymbol{G}_{\sigma s}\hat{\boldsymbol{s}}' + \delta\hat{\boldsymbol{\sigma}}^T \boldsymbol{G}'_{\sigma s}\hat{\boldsymbol{s}} - \delta\hat{\boldsymbol{\sigma}}^T \boldsymbol{H}_{\sigma s}\hat{\boldsymbol{s}}\\ &- \delta\hat{\boldsymbol{\sigma}}^T \boldsymbol{H}_{\sigma\sigma}\hat{\boldsymbol{\sigma}} - \delta\hat{\boldsymbol{s}}^T \boldsymbol{F} \Big) dx - \delta\hat{\boldsymbol{s}}^T \boldsymbol{T} = 0\end{aligned}} \tag{28}$$

where $\widetilde{W} := \left\{ \hat{\boldsymbol{s}} \in H^1(l) : \hat{\boldsymbol{s}}|_{x=0} = \boldsymbol{0} \right\}$, $\widetilde{S} := L^2(l)$, and $\boldsymbol{T} = \int_{H_l} \boldsymbol{P}_s^T \boldsymbol{t} dy$; furthermore

$$L^2(l) := \left\{ \hat{\boldsymbol{\sigma}} : \int_l \hat{\boldsymbol{\sigma}}^T \hat{\boldsymbol{\sigma}} dx < \infty \right\}; \quad H^1(l) := \left\{ \hat{\boldsymbol{s}} : \hat{\boldsymbol{s}}, \hat{\boldsymbol{s}}' \in L^2(l) \right\}$$

We highlight that the derivatives with respect to x are applied only to displacement variables. Moreover, the definition of $\widetilde{W}$ leads to a formulation that essentially satisfies continuity of displacements along the beam axis whereas axial equilibrium is weakly imposed through Equation (28). Finally, the weak formulation (28) is symmetric.

We now suppose that the i-th axial coefficient function $\hat{\gamma}_i$ of a given field $\boldsymbol{\gamma}$ can be approximated as a linear combination of t axis shape functions, stored in a vector $\boldsymbol{N}_{\gamma i} : l \to \mathbb{R}^t$. The t numerical coefficients are collected in the vector $\widetilde{\boldsymbol{\gamma}}_i \in \mathbb{R}^t$. As a consequence:

$$\hat{\boldsymbol{\gamma}} \approx \boldsymbol{N}_\gamma(x)\, \widetilde{\boldsymbol{\gamma}} \tag{29}$$

where

$$\boldsymbol{N}_\gamma =: \begin{bmatrix} \boldsymbol{N}_{\gamma 1}^T & \boldsymbol{0} & \cdots & \boldsymbol{0} \\ \boldsymbol{0} & \boldsymbol{N}_{\gamma 2}^T & \cdots & \boldsymbol{0} \\ \vdots & \vdots & \ddots & \vdots \\ \boldsymbol{0} & \boldsymbol{0} & \cdots & \boldsymbol{N}_{\gamma m}^T \end{bmatrix}; \qquad \widetilde{\boldsymbol{\gamma}} := \begin{Bmatrix} \widetilde{\boldsymbol{\gamma}}_1 \\ \widetilde{\boldsymbol{\gamma}}_2 \\ \vdots \\ \widetilde{\boldsymbol{\gamma}}_m \end{Bmatrix}$$

The FE discretization of the beam model follows from the introduction of the axis shape function approximation (29) into the beam model weak formulation (28):

$$\begin{aligned} \delta J_{HR} = \int_l \Big(& \delta\widetilde{\boldsymbol{s}}^T \boldsymbol{N}_s'^T \boldsymbol{G}_{s\sigma} \boldsymbol{N}_\sigma \widetilde{\boldsymbol{\sigma}} + \delta\widetilde{\boldsymbol{s}}^T \boldsymbol{N}_s^T \boldsymbol{G}'_{s\sigma} \boldsymbol{N}_\sigma \widetilde{\boldsymbol{\sigma}} - \delta\widetilde{\boldsymbol{s}}^T \boldsymbol{N}_s^T \boldsymbol{H}_{s\sigma} \boldsymbol{N}_\sigma \widetilde{\boldsymbol{\sigma}} \\ & + \delta\widetilde{\boldsymbol{\sigma}}^T \boldsymbol{N}_\sigma^T \boldsymbol{G}_{\sigma s} \boldsymbol{N}_s' \widetilde{\boldsymbol{s}} + \delta\widetilde{\boldsymbol{\sigma}}^T \boldsymbol{N}_\sigma^T \boldsymbol{G}'_{\sigma s} \boldsymbol{N}_s \widetilde{\boldsymbol{s}} - \delta\widetilde{\boldsymbol{\sigma}}^T \boldsymbol{N}_\sigma^T \boldsymbol{H}_{\sigma s} \boldsymbol{N}_s \widetilde{\boldsymbol{s}} \\ & - \delta\widetilde{\boldsymbol{\sigma}}^T \boldsymbol{N}_\sigma^T \boldsymbol{H}_{\sigma\sigma} \boldsymbol{N}_\sigma \widetilde{\boldsymbol{\sigma}} - \delta\widetilde{\boldsymbol{s}}^T \boldsymbol{N}_s^T \boldsymbol{F} \Big) dx - \delta\widetilde{\boldsymbol{s}}^T \boldsymbol{N}_s^T \boldsymbol{T} = 0 \end{aligned} \tag{30}$$

Collecting unknown coefficients in a vector and requiring Equation (30) to be satisfied for all possible virtual fields we obtain:

$$\begin{bmatrix} \boldsymbol{0} & \boldsymbol{K}_{s\sigma} \\ \boldsymbol{K}_{\sigma s} & \boldsymbol{K}_{\sigma\sigma} \end{bmatrix} \begin{Bmatrix} \widetilde{\boldsymbol{s}} \\ \widetilde{\boldsymbol{\sigma}} \end{Bmatrix} = \begin{Bmatrix} \widetilde{\boldsymbol{T}} \\ \boldsymbol{0} \end{Bmatrix} \tag{31}$$

where the FE stiffness matrix blocks are defined as follows:

$$\boldsymbol{K}_{s\sigma} = \boldsymbol{K}_{\sigma s}^T := \int_l \left(\boldsymbol{N}_s'^T \boldsymbol{G}_{s\sigma} \boldsymbol{N}_\sigma + \boldsymbol{N}_s^T \boldsymbol{G}'_{s\sigma} \boldsymbol{N}_\sigma - \boldsymbol{N}_s^T \boldsymbol{H}_{s\sigma} \boldsymbol{N}_\sigma \right) dx;$$

$$\boldsymbol{K}_{\sigma\sigma} := -\int_l \boldsymbol{N}_\sigma^T \boldsymbol{H}_{\sigma\sigma} \boldsymbol{N}_\sigma dx; \quad \widetilde{\boldsymbol{T}} := -\int_l \boldsymbol{N}_s^T \boldsymbol{F} dx - \boldsymbol{N}_s^T \big|_{x=\bar{l}} \boldsymbol{T}$$

Looking at the properties of the axis shape functions, we consider the same choices done in (Auricchio et al., 2010) and summarized in Table 3. We notice that the FE solution satisfies:

$$\widetilde{\boldsymbol{s}} = -\left(\boldsymbol{K}_{s\sigma} \boldsymbol{K}_{\sigma\sigma}^{-1} \boldsymbol{K}_{\sigma s} \right)^{-1} \widetilde{\boldsymbol{T}}; \qquad \widetilde{\boldsymbol{\sigma}} = -\boldsymbol{K}_{\sigma\sigma}^{-1} \boldsymbol{K}_{\sigma s} \widetilde{\boldsymbol{s}}$$

In particular, since stresses are $x-$discontinuous, they can be eliminated by static condensation at the element level, reducing the dimension of the global stiffness matrix.

	$\boldsymbol{N}_u$	$\boldsymbol{N}_v$	$\boldsymbol{N}_{\sigma_x}$	$\boldsymbol{N}_{\sigma_y}$	$\boldsymbol{N}_\tau$
$\deg(\boldsymbol{N}_\gamma)$	2	3	1	3	2
x- continuity	yes	yes	no	no	no

Table 3: Polynomial degrees with respect to x of the axis shape functions used in beam FE.

5. Numerical examples

In this section we discuss some numerical results obtained through the FE scheme introduced in Section 4. In particular, we consider the following two test cases.

1. A symmetric tapered beam that shows the beam model accuracy through the comparison of the numerical results with the analytical solutions available in literature.
2. An arch-shaped beam that shows the capability of the beam model to take into account also some phenomena that occur in complex geometries.

Both the examples consider the profile functions defined in Section 3.3 and are implemented in MAPLE software which allows to calculate the FE stiffness matrices using symbolic calculus. Obviously, the same results could be obtained also using numerical-calculus tools together with suitable integration rules.

We introduce the relative error, defined for a given variable γ as:

$$e_\gamma^{rel} := \frac{\left|\gamma - \gamma^{ref}\right|}{\left|\gamma^{ref}\right|} \tag{32}$$

where γ^{ref} is the reference solution (specified for each problem under investigation).

5.1. Symmetric tapered beam

We consider the symmetric tapered beam shown in Figure 3 ($\bar{l} = 10\text{mm}$, $\overline{H}(0) = 1\text{mm}$, and $\overline{H}(\bar{l}) = 0.5\text{mm}$) and we assume $E = 10^5\text{MPa}$ and $\nu = 0.25$ as material parameters. Moreover, the beam is clamped in the initial cross section $\overline{H}(0)$ and a concentrated load $\boldsymbol{Q} = [0, -1]\,\text{N}$ acts in the lower limit of the final cross-section $\overline{H}(\bar{l})$. Finally, we use a homogeneous mesh of 20 elements along the beam axis.

Figure 4 plots the displacement axial coefficients $\{\hat{u}_1; \hat{u}_2\}$ and $\{\hat{v}_1; \hat{v}_2; \hat{v}_3\}$. As expected, only the transver-

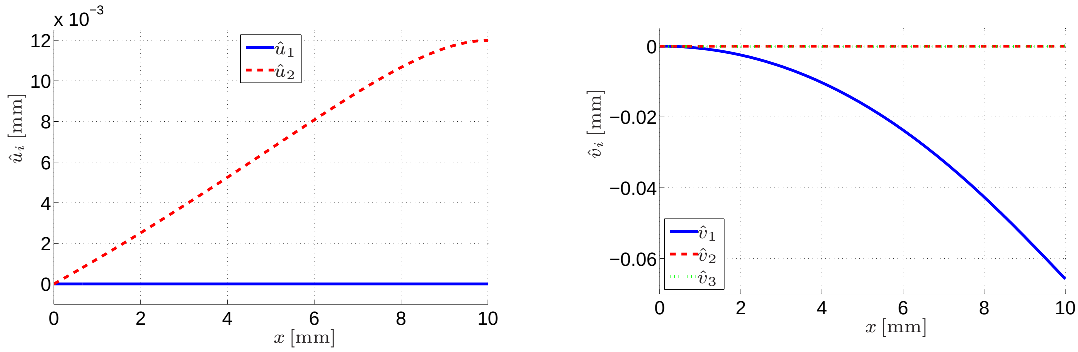

(a) Horizontal displacement, axial coefficient functions $\hat{u}_i \quad i = 1, 2$.

(b) Vertical displacement, axial coefficient functions $\hat{v}_i \quad i = 1, 2, 3$.

Figure 4: Horizontal (Figure 4(a)) and vertical (Figure 4(b)) displacement axial coefficient functions computed for a symmetric tapered beam under shear-bending load.

sal displacement $\hat{v}_1$ and the cross section rotation $\hat{u}_2$ have a significant order of magnitude. Moreover, they have an axial distribution qualitatively similar to the solution of a prismatic cantilever beam.

We define the mean-value of the transversal displacement computed on the final cross section as follows:

$$\overline{v}\,(10) = \int_{H(10)} v\,(x,y)\,dy \tag{33}$$

Table 4 reports the values of $\overline{v}\,(10)$, obtained using different homogeneous meshes and the relative error e_v^{rel} defined in Equation (32). We assume as reference solution v^{ref} the solution of the 2D problem depicted in Figure 3, obtained using the ABAQUS software and a structured mesh of 7680×512 bilinear elements. We

Beam model	$\overline{v}\,(10)$ mm	e_v^{rel}
Beam FE (1 elem.)	-0.0641858	$2.324 \cdot 10^{-2}$
Beam FE (4 elem.)	-0.0656567	$8.522 \cdot 10^{-4}$
Beam FE (20 elem.)	-0.0657294	$2.541 \cdot 10^{-4}$
2D solution (v^{ref})	-0.0657127	-

Table 4: Mean-value of the transversal-displacement evaluated on the final cross-section and obtained considering different axis meshes for a symmetric tapered beam under shear-bending load.

notice that the beam FE proposed in this paper has the capability to predict the maximum displacement with reasonable accuracy even using only 1 element. Moreover, increasing the number of elements, the FE solution converges to the reference solution, leading to satisfying errors for engineering applications.

Figure 5 depicts the stress axial coefficient functions. In particular, Figure 5(c) shows that, far from the

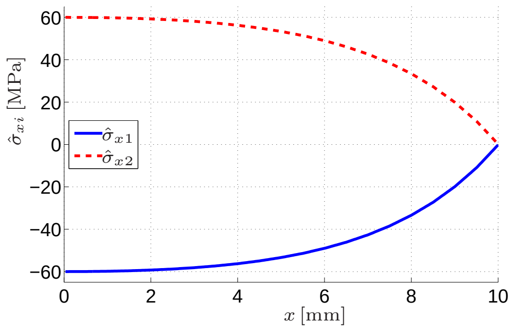

(a) Axial stress, axial coefficient functions $\hat{\sigma}_{xi}\quad i = 1, 2$.

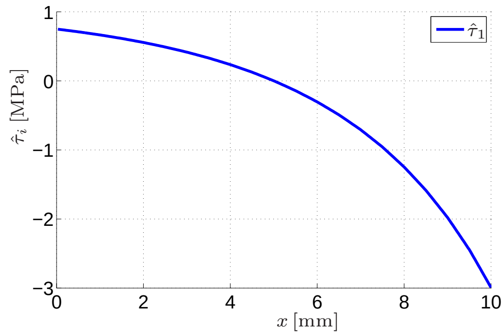

(b) Shear stress, axial coefficient function $\hat{\tau}_1$.

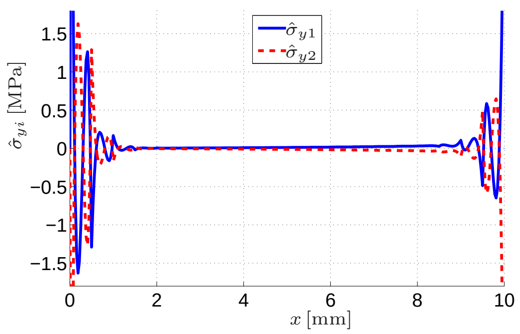

(c) Transversal stress, axial coefficient functions $\hat{\sigma}_{yi}\quad i = 1, 2$.

Figure 5: Stress axial coefficient functions evaluated for a symmetric tapered beam under shear-bending load.

initial and final cross sections, the axial coefficient functions $\hat{\sigma}_{yi}$ $i = 1, 2$ have a negligible order of magnitude if compared to the other stress components. Moreover, close to the initial and final cross sections, the axial coefficient functions $\hat{\sigma}_{yi}$ significantly oscillate. The comparison of different solutions (obtained using different meshes and not reported here for brevity) highlights that the oscillations of the axial coefficient functions occur only in the elements close to the boundaries. These oscillations could be probably explained as an attempt of the beam model to take into account stress concentrations near the domain vertices.

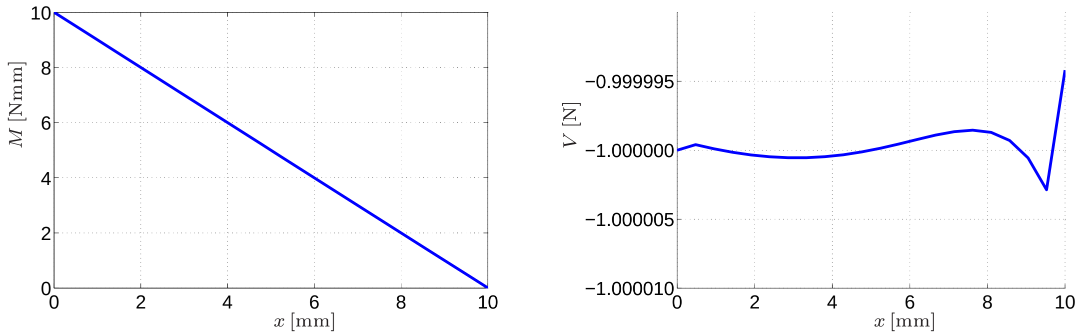

(a) Resulting bending moment, axial distribution $M(x)$.

(b) Resulting shear, axial distribution $V(x)$.

Figure 6: Resulting internal actions evaluated for a symmetric tapered beam under shear-bending load.

Figure 6(a) depict the axis distribution of the bending moment $M(x)$ defined as follows:

$$M(x) = \int_{H(x)} \sigma_x \cdot y \, dy \tag{34}$$

The bending moment distribution $M(x)$ agrees with the classical beam theories: it varies linearly along the axis, vanishing in the final cross section and being equal to $Q \cdot \bar{l} = 10$Nmm in the initial cross section. Instead, the axial coefficient functions $\hat{\sigma}_{x1}$ and $\hat{\sigma}_{x2}$ (Figure 5(a)) are non-linear in order to compensate the change of the cross-section height.

Figure 6(b) plots the axis distribution of resulting shear $V(x)$ defined as follows:

$$V(x) = \int_{H(x)} \tau \, dy \tag{35}$$

The resulting shear $V(x)$ distribution is close to the value $Q = -1$N, even though some oscillations with an amplitude of about $5 \cdot 10^{-6}$N occur. Nevertheless, we conclude that also the resulting shear distribution agrees with the classical beam theories, whereas the axial coefficient function $\hat{\tau}_1(x)$ (Figure 5(b)) is non linear in order to compensate the cross-section changes.

Figure 7 plots the cross section distributions of the computed axial and transversal stresses (σ_x and σ_y, respectively), compared with the corresponding quantities obtain using the solution detailed in (Timoshenko and Goodier, 1951, Section 35). The label *num* indicates the numerical solution obtained through the FE introduced in Section 4, whereas the label *ref* indicates the solution of (Timoshenko and Goodier, 1951, Section 35). Finally, to exclude boundary effects, we consider the cross section corresponding to $x = 5$, and denoted as $H(5)$. We highlight the good agreement between numerical results and the reference solution.

The shear cross section distribution τ requires some additional remarks. Figures 8(a), 8(b), and 8(c) plot the shear distributions computed on the cross sections $H(2.5)$, $H(5)$, and $H(7.5)$.

In Figures 8(a) and 8(c), we observe a very good agreement between numerical and reference solutions. Concerning Figure 8(b), we notice that the reference solution has a high frequency component that the numerical solution is unable to capture. This is due to the low-order degree of the profile functions adopted in the model. However, we notice that the error is of a reasonable magnitude. Finally, Figure 8(d) depicts the absolute error in the three considered cross sections. Again, the numerical solutions display a satisfactory agreement with the reference solutions.

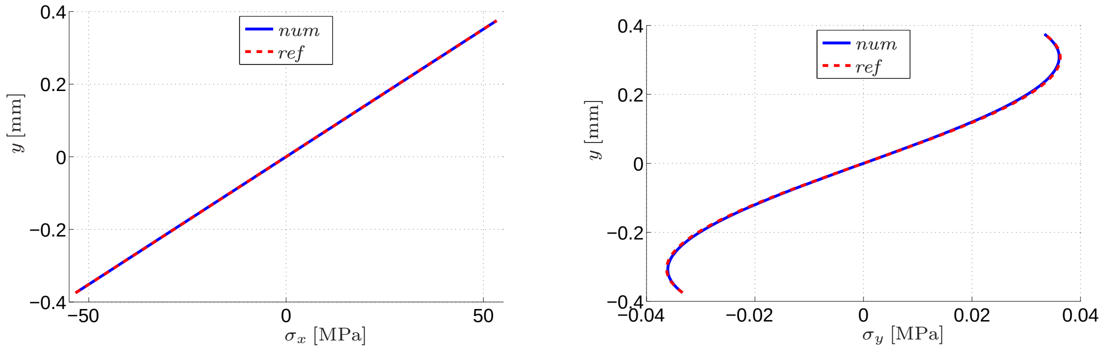

(a) Axial stress σ_x cross-section distribution.

(b) Transversal stress σ_y cross-section distribution.

Figure 7: Axial (Figure 7(a)) and transversal (Figure 7(a)) stress cross-section distributions, evaluated in the cross section $H(5)$ for a symmetric tapered beam under shear-bending load.

5.2. Arch shaped beam

We now consider the arch shaped beam shown in Figure 9. The lower and the upper boundaries are defined respectively as:

$$h_l(x) := -\frac{1}{50}x^2 + \frac{1}{5}x - \frac{1}{2}; \quad h_u(x) := \frac{1}{10} \tag{36}$$

Moreover, the beam is clamped in the initial cross section and loaded on the final cross section with a constant axial load distribution $\boldsymbol{t}|_{H_l} = [1, 0, 0]^T$ N/mm. A homogeneous mesh of 20 elements is used and we adopt the profile functions introduced in Equations (24) and (25).

Figure 10 depicts the displacement axial coefficients. We highlight that the solution shows significant transversal displacement (see $\hat{v}_1$ in Figure 10(b)) and cross-section rotation (see $\hat{u}_2$ in Figure 10(a)) even if only an axial load is applied. The displacement solutions indicate that the beam model and the corresponding FE take into account the coupling between axial and bending equations, a consequence of the domain lack of symmetry with respect to the $x-$axis.

We define the mean-value of the axial displacement computed on the final cross section as follows:

$$\overline{u}(10) = \int_{H(10)} u(x, y)\, dy \tag{37}$$

Table 5 reports the values of $\overline{u}(10)$ and $\overline{v}(10)$ (defined in Equation (33)), obtained using different meshes and the corresponding relative errors e_v^{rel} and e_u^{rel} defined in Equation (32). We compute the reference solution by means of the ABAQUS software, considering the full 2D problem and using a structured mesh of 10240×256 bilinear elements. The results highlight that the proposed model is effective in the prediction of

Beam model	$\overline{v}(10)$ mm	e_v^{rel}	$\overline{u}(10)$ mm	e_u^{rel}
Beam FE (1 elem.)	0.016753	$9.247 \cdot 10^{-1}$	0.0009789	$9.102 \cdot 10^{-1}$
Beam FE (4 elem.)	0.219495	$1.322 \cdot 10^{-2}$	0.0120440	$1.052 \cdot 10^{-1}$
Beam FE (20 elem.)	0.222434	$8.991 \cdot 10^{-6}$	0.0108971	$4.588 \cdot 10^{-5}$
2D solution (v^{ref}, u^{ref})	0.222436	-	0.0108976	-

Table 5: Mean-value of the transversal and axial displacements computed on the final cross section and obtained considering different meshes for an arch shaped beam under axial load.

the displacements. However, the very rough single-element discretisation doe not yet provide a satisfactory result in this case.

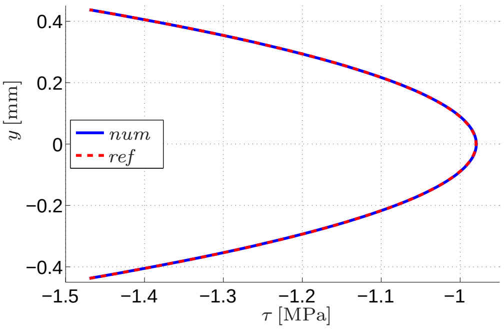

(a) Shear τ cross-section distribution, evaluated in the cross section $H\,(2.5)$.

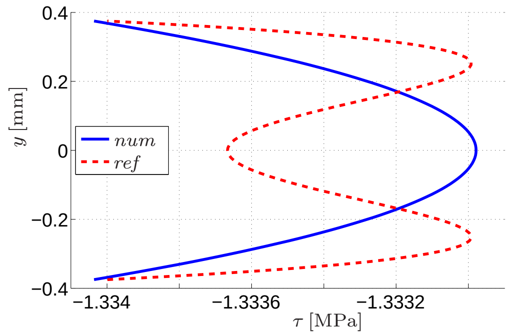

(b) Shear τ cross-section distribution, evaluated in the cross section $H\,(5)$.

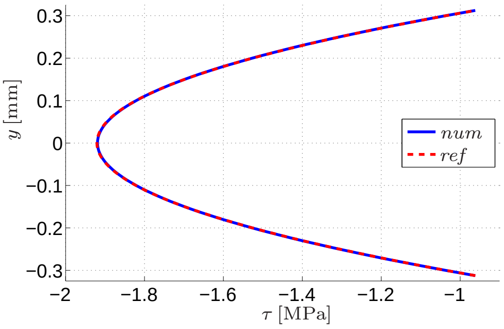

(c) Shear τ cross-section distribution, evaluated in the cross section $H\,(7.5)$.

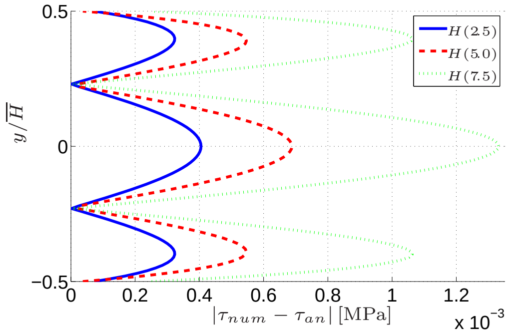

(d) Absolute error $\left|\tau^{num} - \tau^{ref}\right|$ evaluated in different cross sections ($H\,(2.5)$, $H\,(5.0)$, and $H\,(7.5)$).

Figure 8: Cross-section shear distributions (Figures 8(a), 8(b), and 8(c)) evaluated in the cross-sections $H\,(2.5)$, $H\,(5.0)$, and $H\,(7.5)$) respectively for a symmetric tapered beam under shear-bending load and related absolute errors (Figure 8(d)).

Figure 11 depicts the stress axial coefficients, Figure 12(a) depicts the resulting axial stress defined in (38), and Figure 12(b) depicts the eccentricity, defined in (39):

$$N\,(x) = \int_{H(x)} \sigma_x \, dy \tag{38}$$

$$e\,(x) := \frac{M\,(x)}{|\boldsymbol{t}|} \tag{39}$$

In particular, *num* denotes the eccentricity computed considering the FE solution, whereas *ref* denotes the analytical eccentricity (it coincides with the positions of the cross section barycentre). We notice that the stress axial distributions are highly non linear, whereas the resulting axial load is constant and equal to the resulting load. Figure 12(a) highlights a small error, of the order of the $5 \cdot 10^{-3}$N, in the resulting axial stress. Moreover, the numerical eccentricity $e^{num}(x)$ coincides with the analytical eccentricity $e^{ref}(x)$. As a consequence, we conclude that the proposed beam model has the capability to model the coupling of axial load and bending moment. Furthermore, we highlight that the coupling factors are automatically obtained from the dimensional reduction procedure illustrated in Section 3.

Figure 13 depicts the cross section distributions of the stresses σ_x, σ_y, and τ. The label *num* indicates the numerical solution obtained through the FE introduced in Section 4, whereas the label *ref* indicates the 2D ABAQUS solution. In order to exclude boundary effects, we consider the cross section corresponding to the axis coordinate $x = 7.5$ and denoted as $H\,(7.5)$. We highlight the good agreement between numerical results and the reference solution.

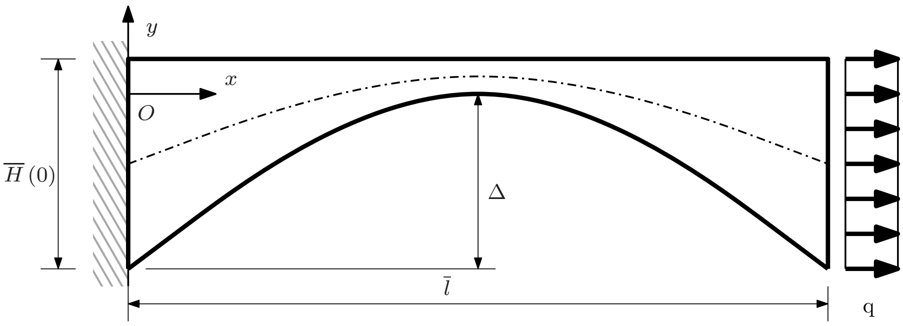

Figure 9: Arch shaped beam: $\bar{l} = 10$mm, $\Delta = 0.5$mm, $\overline{H}\left(\bar{l}\right) = \overline{H}(0) = 0.6$mm, $q = 1$N/mm, $E = 100000$MPa, and $\nu = 0.25$.

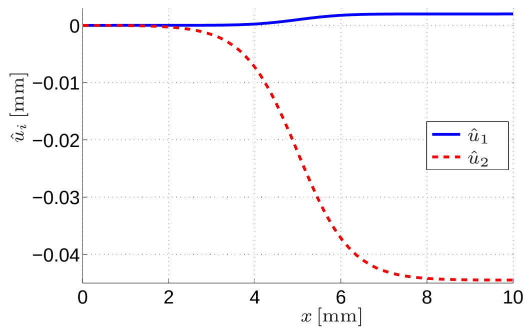

(a) Horizontal displacement, axial coefficient functions $\hat{u}_i \quad i = 1, 2$.

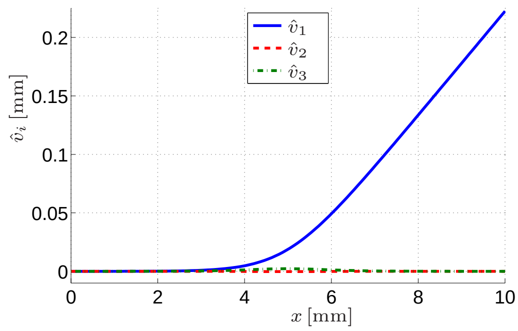

(b) Vertical displacement, axial coefficient functions $\hat{v}_i \quad i = 1, 2, 3$.

Figure 10: Horizontal (Figure 10(a)) and vertical (Figure 10(b)) displacement axial coefficient functions, evaluated for an arch shaped beam under axial load.

6. Stiffness-matrix condition-number

In this section we provide some information about the influence of the geometry parameters on the beam FE introduced in Section 4. We here consider the condition number of the FE stiffness matrix as a possible indicator of the range of applicability of our numerical scheme.

We recall that the condition number of a given matrix $\boldsymbol{A}$ is defined as:

$$\mathrm{cond}\left(\boldsymbol{A}\right) := \|\boldsymbol{A}\| \cdot \|\boldsymbol{A}^{-1}\| \tag{40}$$

We here choose the norm:

$$\|\boldsymbol{A}\| := \max_{i=1\ldots n} \left\{ \sum_{j=1}^{n} |a_{ij}| \right\} \tag{41}$$

Figure 16(a) depicts the condition number computed for a prismatic beam, versus the number of elements, for different values of beam slenderness $\bar{l}/\overline{H}$. In particular, we notice that the condition number gets larger as the beam becomes more slender.

Figure 16(b) depicts the condition number computed versus the number of elements for the non-symmetric beam of Figure 14, and for different values of Δ. Here, Δ is defined as the difference between the initial and final cross section heights. Furthermore, the average of the cross section height is kept constant in all the considered cases, as as shown in Table 6. We notice that the condition number becomes larger as Δ gets larger.

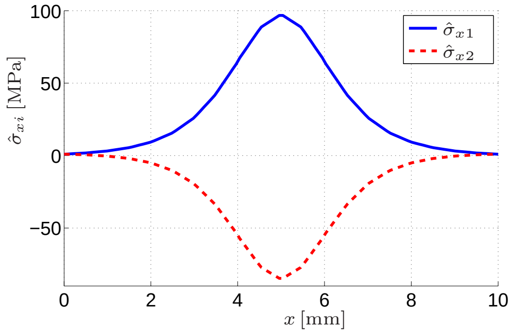

(a) Axial stress, axial coefficient functions $\hat{\sigma}_{xi}$ $\quad i = 1, 2$.

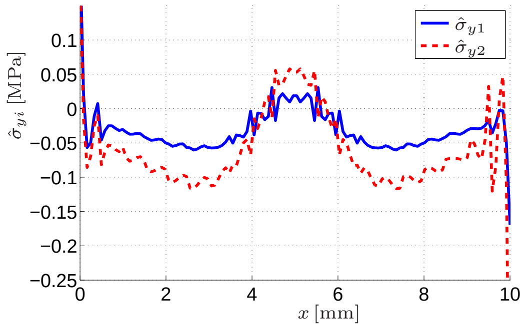

(b) Transversal stress, axial coefficient functions $\hat{\sigma}_{yi}$ $\quad i = 1, 2$.

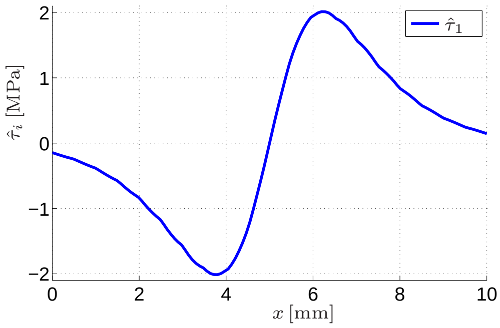

(c) Shear stress, axial coefficient functions $\hat{\tau}_1$.

Figure 11: Axial (Figure 11(a)), transversal (Figure 11(b)), and shear (Figure 11(c)) stress axial coefficient functions, evaluated for an arch shaped beam under axial load.

As a final example, we consider a beam with a wave-like shape of the lower boundary, as shown in Figure 15.

In this case, we choose the maximum slope $h'_m := \max_{x \in l} (|h'_l|)$ as relevant geometric parameter. We notice that h'_m determines the number of waves in the lower boundary description, see Table 7. Figure 16(c) shows the condition number versus the number of elements, for different choices of h'_m. We observe that h'_m does not significantly affect the condition number, at least for the cases of practical interest.

7. Conclusions

In this paper we developed a planar, non-prismatic beam model based on a mixed variational approach. More precisely, we formulated the 2D elastic problem through the Hellinger-Reissner functional, with the goal to accurately describe the stress profiles. In Section 3 we applied the dimensional reduction procedure

Δ	$\overline{H}(0)$	$\overline{H}(l)$	h'_l
0.0	5.50	5.50	0.00
0.1	5.55	5.45	0.01
1.0	6.00	4.00	0.10
5.0	8.00	3.00	0.50
10.0	10.50	0.50	1.00

Table 6: Non-symmetric tapered beams, parameter definitions for the considered examples.

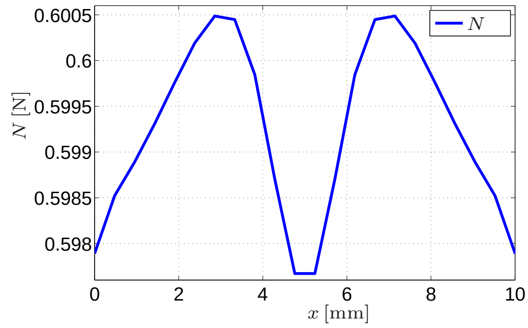

(a) Resulting axial force $N(x)$.

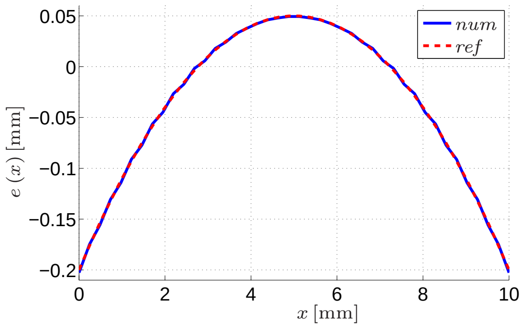

(b) Resulting eccentricity $e(x)$.

Figure 12: Resulting axial force (Figure 12(a)) and eccentricity (Figure 12(b)), evaluated for an arch shaped beam under axial load.

wave number	λ	h'_m
0	-	0
1	10.00	⅛
2	5.00	¼
4	2.50	½
8	1.25	1

Table 7: Non-prismatic beams, parameter definitions for the considered examples.

that leads to the formulation of the non-prismatic beam model. In Section 4 we developed the non-prismatic beam FE. In Section 5 we gave some numerical results that assessed the efficiency of the proposed model. Finally, in Section 6 we provided some indications about the influence of the geometry parameters on the effectiveness of the proposed beam FE.

Numerical results show that the beam model and the corresponding FE are capable to accurately approximate the analytical results available in literature. Moreover, the model takes into account the coupling of axial stress and bending moment since the coupling terms naturally arise from the modeling procedure.

Future developments of this work could include the extension to the 3D case and to multilayer, non-homogeneous beams.

References

Auricchio, F., G. Balduzzi, and C. Lovadina (2010). A new modeling approach for planar beams: finite-element solutions based on mixed variational derivations. *Journal of Mechanic of Materials and Structures 5*, 771–794.

Banerjee, J. R. and F. W. Williams (1985). Exact Bernoulli-Euler dynamic stiffness matrix for a range of tapered beams. *International Journal for Numerical Methods in Engineering 21*(12), 2289–2302.

Banerjee, J. R. and F. W. Williams (1986). Exact Bernoulli-Euler static stiffness matrix for a range of tapered beam-columns. *International Journal for Numerical Methods in Engineering 23*, 1615–1628.

Boley, B. A. (1963). On the accuracy of the Bernoulli-Euler theory for beams of variable section. *Journal of Applied Mechanics 30*, 374–378.

Hodges, D. H., J. C. Ho, and W. Yu (2008). The effect of taper on section constants for in-plane deformation of an isotropic strip. *Journal of Mechanic of Materials and Structures 3*, 425–440.

Hodges, D. H., A. Rajagopal, J. C. Ho, and W. Yu (2010). Stress and strain recovery for the in-plane deformation of an isotropic tapered strip-beam. *Journal of Mechanic of Materials and Structures 5*, 963–975.

Kantorovich, L. and V. Krylov (1958). *Approximate methods of higher analysis* (Third ed.). P. Noordhoff LTD.

Kitipornchai, S. and N. S. Trahair (1975). Elastic behavior of tapered monosymmetric I-beams. *Journal of the structural division 101*, 11479–11515.

Li, G.-Q. and J.-J. Li (2002). A tapered Timoshenko-Euler beam element for analysis of steel portal frames. *Journal of Constructional Steel Research 58*, 1531–1544.

Rajagopal, A. and D. H. Hodges (2014). Asymptotic approach to oblique cross-sectional analysis of beams. *Journal of Applied Mechanics 81*(031015), 1–15.

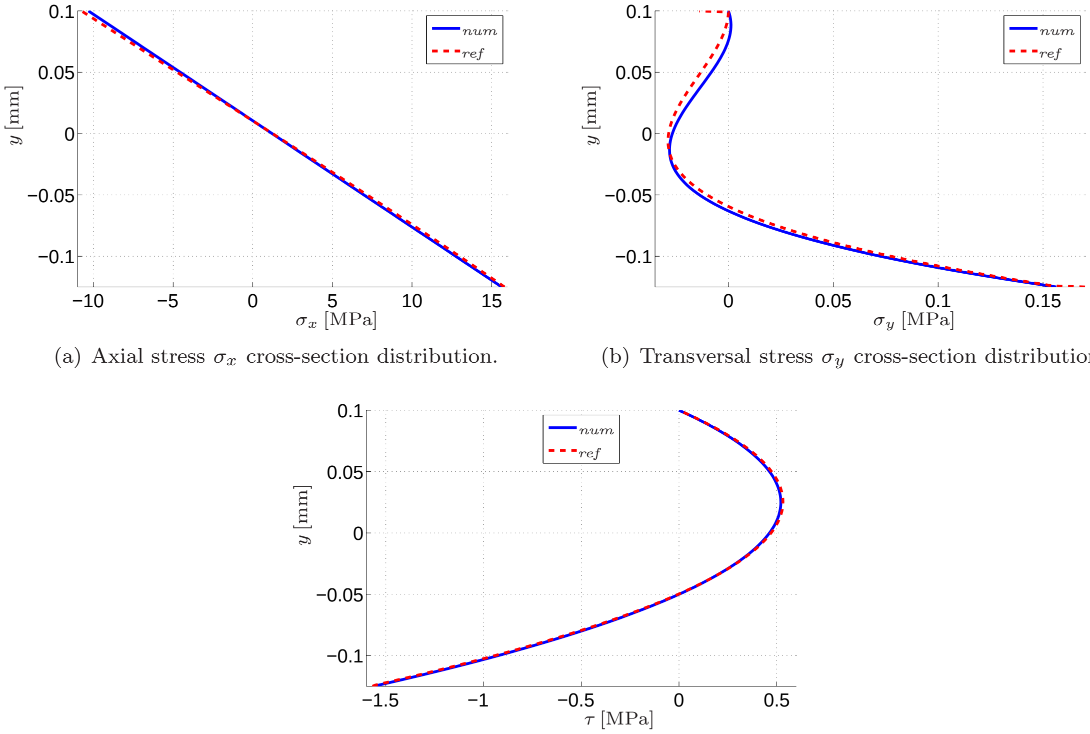

(a) Axial stress σ_x cross-section distribution.

(b) Transversal stress σ_y cross-section distribution.

(c) Shear stress τ cross-section distribution.

Figure 13: Axial (Figure 13(a)), transversal (Figure 13(a)), and shear (Figure 13(c)) stresses cross section distributions, computed in the cross section H (7.5) for an arch shaped beam under axial load.

Rajagopal, A., D. H. Hodges, and W. Yu (2012). Asymptotic beam theory for planar deformation of initially curved isotropic strips. *Thin-Walled Structures 50*, 106.115.

Timoshenko, S. and J. N. Goodier (1951). *Theory of Elasticity* (Second ed.). McGraw-Hill.

Vinod, K. G., S. Gopalakrishnan, and R. Ganguli (2007). Free vibration and wave propagation analysis of uniform and tapered rotating beams using spectrally formulated finite elements. *International Journal of Solids and Structures 44*, 5875–5893.

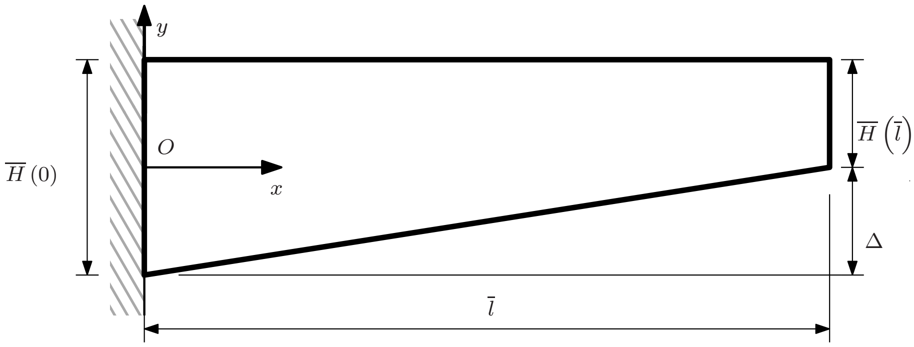

Figure 14: Non-symmetric tapered beam: $\bar{l} = 10$mm, $\overline{H}(0) = \overline{H}\left(\bar{l}\right) + \Delta$, $E = 100000$MPa, and $\nu = 0.25$.

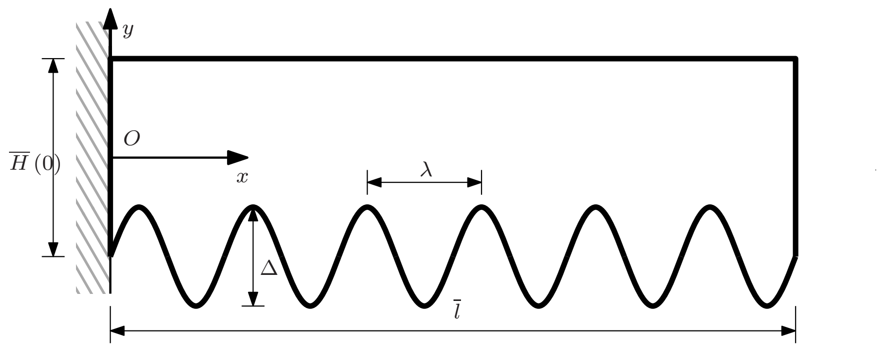

Figure 15: Non-prismatic beam: $\bar{l} = 10$mm, $\overline{H}(0) = 1$mm, $\Delta = 0.46875$mm, $E = 100000$MPa, and $\nu = 0.25$.

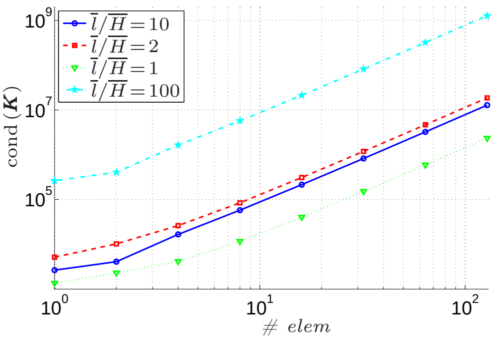

(a) Condition number, evaluated for a prismatic beam with different ratio $\bar{l}/\overline{H}$.

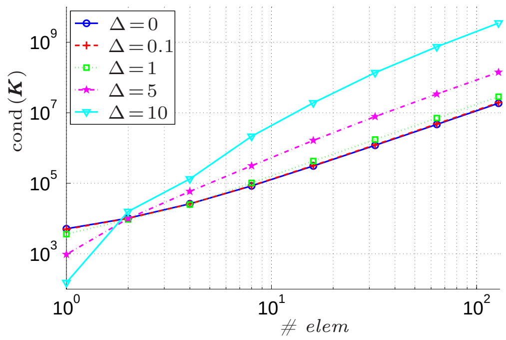

(b) Condition number, evaluated for a non-symmetric tapered beam with different taper slope.

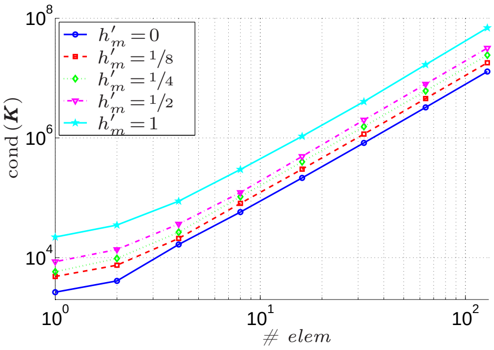

(c) Condition number, evaluated for a non-prismatic beam with different boundary slope.

Figure 16: Stiffness matrix condition number evaluated for prismatic beams (Figure 16(a)), non-symmetric tapered beams (Figure 16(b)), and non-prismatic beams (Figure 16(c)).